Journal of Hydrology 533 (2016) 603–614

Contents lists available at ScienceDirect

Journal of Hydrology

journal homepage: www.elsevier.com/locate/jhydrol

Overland flow from plant patches: Coupled effects of preferential infiltration, surface roughness and depression storage at the semiarid Patagonian Monte

María J. Rossi [a,b,*], Jorge O. Ares [a]

[a] National Patagonic Center, National Council for Scientific and Technological Research, Argentina (CONICET), Puerto Madryn, Argentina
[b] Department of Animal and Range Sciences, New Mexico State University, Las Cruces, NM, USA

ARTICLE INFO

Article history:
Received 24 September 2015
Received in revised form 14 December 2015
Accepted 15 December 2015
Available online 21 December 2015
This manuscript was handled by Corrado Corradini, Editor-in-Chief

Keywords:
Plant patches
Runoff redistribution
Preferential flow
Micro-topography
Depression storage
Hydrological model

SUMMARY

The objective of this study is to characterize and quantify the overland flow generated from the plant patch areas of spotted vegetation toward the immediate surrounding bare ground including the coupled effects of preferential infiltration, surface roughness and depression storage. To this aim a series of overland flow plot experiments were designed in areas of the Patagonian Monte where evidence of patch-to-soil overland flow was observed. The experiments produced data on the plot micro-topography and physical properties of the soil, root density and the frictional parameters of the overland flow as well as the extent of the areas of water depression storage. The obtained data were used to calibrate a spatial-explicit (CREST) hydrological model of the flows and pathways generated by stemflow and throughfall during characteristic storms in the area. Good agreement between the model estimates and the measured data was found. This work provides physically-based metrics of runoff redistribution from the plant patch areas toward the immediate surrounding bare soil areas, including the effect of plant roots and depression storage as influenced by various shapes of the plant patch slopes. It is concluded that water transport can result from stemflow and throughfall at the patch areas during typical rainfall events at the semiarid Patagonian Monte. Implications of this phenomenon in the surface distribution of water, nutrients and seeds may feasibly follow.

1. Introduction

The distribution of the vegetation cover in arid and semiarid environments around the world occurs in patterns that can be either spatially periodic or random, in regular bands, spotted clumps, gap patterns and labyrinths (Bisigato et al., 2009; Couteron and Lejeune, 2001; Klausmeier, 1999; Malam Issa et al., 2011; von Hardenberg et al., 2001). In these systems the effect of vegetation generates contrasting differences in the physical characteristics of the soil beneath plant patches and neighboring bare soil (Casermeiro et al., 2004; Merino-Martín et al., 2015). In semi-arid regions a high proportion of fine roots are found in the superficial soil layers (Gill et al., 1999; Silva and Rego, 2003). Decayed and fresh root channels generate soil macroporosity and contribute to preferential infiltration flow resulting in higher infiltration than expected as based on the textural properties of the surface soil (van Schaik, 2009). The combined effect of the plant canopy and ground cover conditions in vegetated patches has been proved to be important in regulating runoff processes (Archer et al., 2012; Bautista et al., 2007; Pueyo et al., 2013; Wainwright et al., 2002), as they are responsible for rainfall interception and the decrease of raindrop impact energy, while ground cover promotes rainfall infiltration into the soil and reduces overland flow velocities (Vásquez-Méndez et al., 2010).

Stemflow and throughfall are highly variable between and within types of vegetation (Llorens and Domingo, 2007) and vary for a same canopy with the peak intensity of the rainfall events (Dunkerley, 2013). The interception of precipitation by a shrub canopy promotes the accumulation of surface water from stemflow at the plant base (Abrahams et al., 2003) and from throughfall which reaches ground by passing through or dripping from the plant structures. These processes also influence overland flow paths. When the intensity of precipitation exceeds the water infiltration rate, the excess of water initially fills surface depressions and then flows downslope over the soil surface (Mao et al., 2008; Rango et al., 2006).

* Corresponding author at: National Patagonic Center, National Council for Scientific and Technological Research, Puerto Madryn, Argentina.
E-mail address: rossi@cenpat-conicet.gob.ar (M.J. Rossi).

http://dx.doi.org/10.1016/j.jhydrol.2015.12.028
0022-1694/

Nomenclature

Acronyms

BS	bare soil
DEM	digital elevation map
RP	runoff plume
TDI	Tension Disk Infiltrometer
TDR	Time-Domain Reflectometer
VS	vegetated soil
S	sample

Variables

υ	kinematic viscosity ($mm^2\ s^{-1}$)
α	inverse of the air-entry parameter (kPa^{-1})
θ_g	gravimetric soil moisture (g)
θ_i	antecedent water content of the soil ($mm^3\ mm^{-3}$, mm)
θ_r	residual volumetric moisture ($mm^3\ mm^{-3}$)
θ_s	saturated moisture content ($mm^3\ mm^{-3}$)
θ_v	volumetric soil moisture ($mm^3\ mm^{-3}$)
$\Delta A(t)$	instantaneous expansion of RP area during the *n-th* time interval (mm^2)
$A(t_n)$	instantaneous RP area at *n-th* time interval (mm^2)
A_{BS}	area of RP over bare soil surrounding plant patch (mm^2)
A_{DS}	depression storage area (mm^2)
A_{end}	RP total area at the end of the flow experiment (mm^2)
A_{VS}	area of RP occupied by plant patch (mm^2)
d^*	average depth of the RP (mm)
DS	depression storage (%) (Base: total runoff plume (RP) area)
F	accumulated infiltration (mm)
$f(t_\infty)$	steady state infiltration rate ($mm\ s^{-1}$)
$f(t)$	instantaneous infiltration rate at *n-th* time interval ($mm\ s^{-1}$)
$IN(t)$	instantaneous total infiltration flow at *n-th* time interval ($mm^3\ s^{-1}$)
$IN_{pref}(t)$	instantaneous preferential infiltration flow at *n-th* time interval ($mm^3\ s^{-1}$)
$IN_{sat}(t)$	instantaneous saturated infiltration flow at *n-th* time interval ($mm^3\ s^{-1}$)
$IN_{unsat}(t)$	instantaneous un-saturated infiltration flow at *n-th* time interval ($mm^3\ s^{-1}$)
$K_h(\theta(t))$	variable hydraulic conductivity ($mm\ s^{-1}$)
K_{sat}	saturated hydraulic conductivity ($mm\ s^{-1}$)
$K_{sat}BS$	K_{sat} estimated by the TDI at the patch surrounding area ($mm\ s^{-1}$)
$K_{sat}VS$	K_{sat} estimated by the TDI at the central area of the plant patch ($mm\ s^{-1}$)
L	soil tortuosity connectivity
Q_o	water stored at the RP as overland flow (mm^3)
$Q_o(t)$	instantaneous overland flow at *n-th* time interval ($mm^3\ s^{-1}$)
Q_v	water stored at the upper vadose zone (mm^3)
r	TDI disk radius (mm)
Re	Reynolds number
$s(t_n)$	terrain height change along the contour of the RP area at time t (mm)
s^*	average terrain height change along the contour of the RP (mm)
SBD	soil bulk density ($g\ cm^{-3}$)
SG	gravel content in soil % (Base: weight of dry (105°), sieved (2 mm mesh) soil)
SR	amount of roots in soil % (Base: weight of dry (105°), sieved (2 mm mesh) soil)
SS	sand content in soil % (Base: weight of dry (105°), sieved (2 mm mesh) soil)
t	time (min)
v^*	mean overland flow velocity ($mm\ s^{-1}$)
$W(t)$	instantaneous water inflow rate ($mm^3\ s^{-1}$)
$z_f(t)$	instantaneous water infiltration depth at *n-th* time interval (mm)
σ_s	surface roughness (mm)
$\psi_f(\theta)$	suction at the wetting front of infiltration (mm)

As infiltration rates are greater under plant canopies, at large spatial scales more surface runoff is generated at bare interspaces than at areas with plant cover. Extensive research in semiarid regions with banded shrubby vegetation and mulga environments (Bromley et al., 1997; Cornet et al., 1992; Dunkerley and Brown, 1995; Dunkerley, 2002; Ludwig et al., 1999; Moreno-de las Heras et al., 2012) and at semiarid patchy landscapes (Li et al., 2008; Reid et al., 1999; Rango et al., 2006) showed that the combination of bare ground and vegetation patches creates a spatial mosaic of sources and sinks where bare ground typically carries runoff and sediments (source) and vegetation traps water and sediments (sink).

At a finer spatial scale (1–2 m) field evidence shows that under circumstances at semiarid areas overland flow can also occur from the plant patch areas to the surrounding bare soil (Fig. 1) in apparent inversion of the well-known source-sink trend observed at large spatial scales. Some experimental work has also been aimed to characterize runoff within (Archer et al., 2012) and around (Vásquez-Méndez et al., 2010) plant patches. Since these flows may imply spatial redistribution of water, nutrients and seeds (Bochet, 2015; Thompson et al., 2014) between patches and bare soil around, there seems to be a need for studies involving direct measurement of water fluxes at this scale aimed to understand the water transport processes at vegetation patches at relatively flat spotted semiarid landscapes (Harman et al., 2014; Thompson et al., 2011).

The objective of this study is to characterize and quantify the overland flow generated from the plant patch areas of spotted vegetation toward the immediate surrounding bare ground including the coupled effects of preferential infiltration, surface roughness and depression storage within the plant patch areas. To this aim the coupled overland and infiltration flows and pathways generated by stemflow and throughfall under vegetation patches were simulated with a spatial-explicit (CREST) calibrated hydrological model. The CREST model input parameters were estimated by sampling soil properties, characterizing the micro-topography, and estimating dynamic water mass balances of 12 field overland flow experiments with different vegetation patches.

2. Materials and methods

2.1. Site description

The experiments here presented were performed at the Wildlife Refuge "La Esperanza" (Fig. 2; UL corner: S: −42.16972, W: −64.9934; LR corner: S: −42.2144, W: −64.96193), a representative site of the Monte Phyto-geographical Province in Argentina, in northern Patagonia (Abraham et al., 2009).

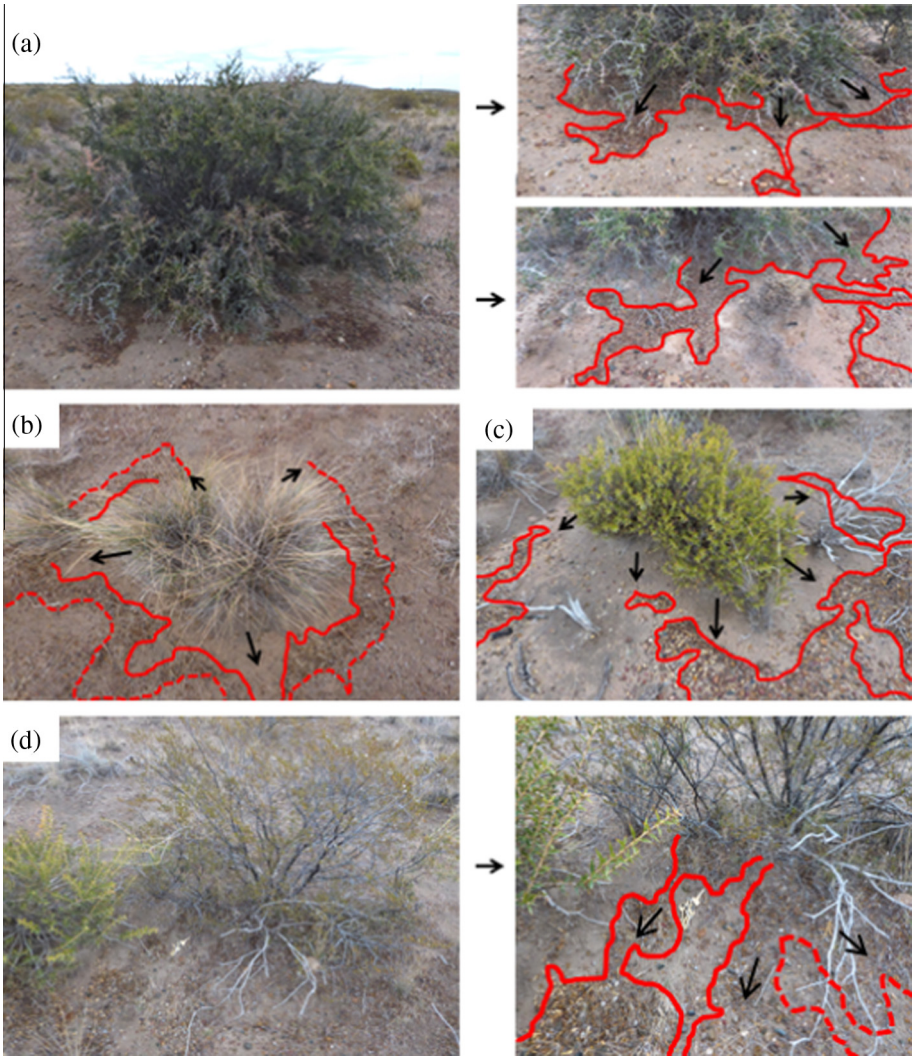

Fig. 1. View of litter and sediment rills and dikes (delimited by red lines) generated by overland flow shed from various plant patches to the immediate surrounding bare soil at the Patagonian Monte. (a) *Schinus S. johnstonii* (frontal and back view insets), (b) *Pappostipa speciosa* and (c) *Chuquiraga avellanedae Lorentz*, (d) *Larrea divaricata Cav*. (For interpretation of the references to color in this figure legend, the reader is referred to the web version of this article.)

The climate is arid and temperate. The mean annual temperature is 13.4 °C and the mean annual precipitation is 258 mm (1995–2004). Although most of the rainfall occurs during the cold season (April to September in the southern hemisphere), heavy rainfall events are more common during the warm season.

The shrub and dwarf shrub dominant species are Larrea divaricata Cav., Chuquiraga avellanedae Lorentz, Schinus johnstonii and Nassauvia fuegiana. Main grasses are Pappostipa speciosa, Stipa tenuis Phil., and Poa ligularis Nees ex Steud. These latter species are found in the mounds, associated with shrubs or distributed in small patches or as scattered plants in the inter-shrub area (Ares et al., 1990; Bertiller et al., 1991; Chartier and Rostagno, 2006; Soriano, 1950).

Soils are a complex of Typic Petrocalcids–Typic Haplocalcids (Soil Survey Staff, 1999) with a fractured calcium carbonate layer from 0.45 to 1 m below the soil surface (del Valle et al., 1998). Upper soil texture types (USDA) are sandy or loamy sand (Rossi and Ares, 2012b). The dominant aspect of the area is of nearly flat soil surfaces with interspersed small mounds associated to shrub–grass patches. A desert pavement occurs at some degraded shrub interspaces where partial topsoil stripping occurred. Wind erosion has probably been an important process in molding this mound–inter-mound pattern. Water erosion seems to be the main recent geomorphic process as indicated by conspicuous rills and dikes of sediment and litter (Chartier and Rostagno, 2006).

2.2. Sampling and measurement of soil properties

Soil properties were sampled at 12 plots (≅0.8 × 0.8 m) with one plant patch each by taking three core samples (diameter: 4 cm, total depth: 18 cm) at increasing distance from the patch central area. One of the cores was extracted from the contiguous or immediate bare soil (BS) areas surrounding the patches. The soil cores were brought to the laboratory in sealed containers and used to estimate gravimetric moisture (θ_g) and the corresponding volumetric (θ_v) equivalent through correction with soil bulk density.

Each core sample was divided to determine the soil properties at 3 different depth intervals (0–3, 3–9, 9–18 cm). Roots (*SR*) and gravel (*SG*) samples were separated from the soil by sieving through a 2 mm mesh, washed, dried at 70 °C for 48 h, and weighed (Böhm, 1979). The texture of the sieved soil was characterized with Lamotte's 1067 texture kit (LaMotte Co., Chestertown) calibrated with replicate estimates obtained at two reference laboratories (National Patagonic Center, National University of the South, Argentina) with the Robinson's protocol (Gee and Bauder, 1986).

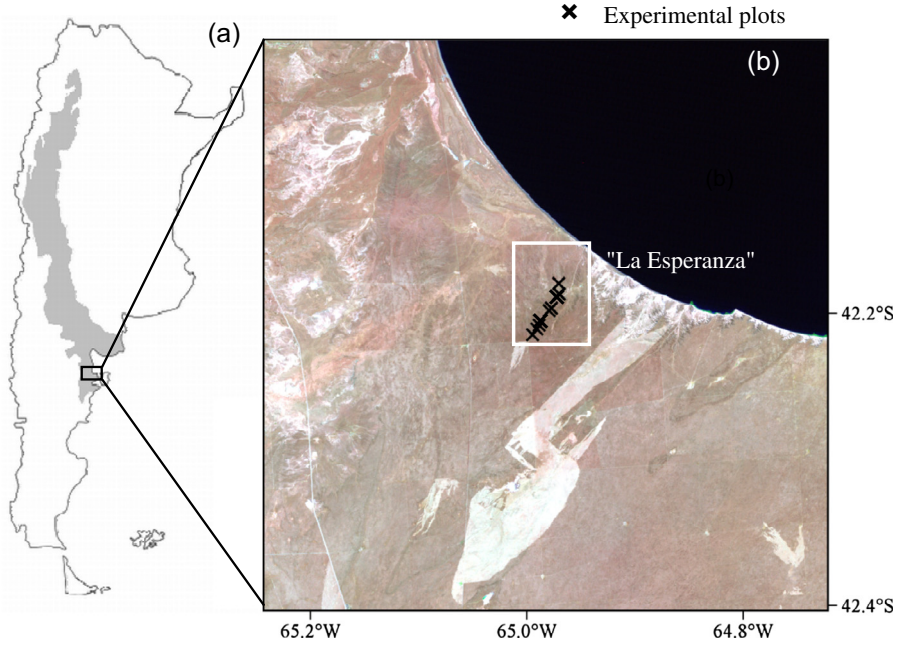

Fig. 2. (a) Location of the field site within the Monte Phyto-geographical Province in Argentina. (b) Landsat 5 TM path-row: 227-89 (22/10/2011 R:7 G:4 B:2) of the site with the location of the experimental plots.

Two soil bulk density (*SBD*) measurements were made at each plot through the excavation method (ISO 11272, 1998). One measurement was located at the central area of the plant patches, and the other at the immediate surrounding BS area.

Infiltration tests to obtain time-varying infiltration curves were performed at the central area of the plant patches and immediate surrounding BS areas using a Tension Disk Infiltrometer (TDI), (diameter = 45 mm, Decagon Devices, Pullman, WA). Test infiltration surfaces were prepared by adding a 3 mm layer of silica sand (0.1–0.5 mm grain diameter) on the soil surface to improve hydraulic contact between the soil and the infiltrometer disc. The saturated hydraulic conductivity (K_{sat}) was estimated through the Wooding's (1968) model:

$$f(t_\infty) = K_{sat}[(1 + 4/(\alpha \cdot \pi \cdot r))e^{(\alpha \cdot h)}] \quad (1)$$

where $f(t_\infty)$ is the steady state infiltration rate at the TDI working tension h (mm s^{-1}), α is the inverse of the air-entry (kPa^{-1}) and r is the TDI disk radius (mm).

Steady infiltration rates were calculated by fitting an exponential curve (TableCurve 2D v.5.01, Systat Software Inc., San Jose, California) to the sequence of $f(t)$ data at 30 s intervals, where:

$$f(t) = a + bx^c \quad (2)$$

where $f(t)$ is the instantaneous infiltration rate (mm s^{-1}) and $a = f(t_\infty)$.

Multiple stepwise linear regression were performed with the Statistica software package (StatSoft Inc., Tulsa, Oklahoma) was used to analyze the relations of K_{sat} measured at the plant patches and the soil properties.

2.3. Overland flow experiments

Overland flow was generated through technical means at the plots described in Section 2.2 to estimate and evaluate the parameters that characterize it at vegetation patches with due regard to the simultaneous effect of preferential infiltration, depression storage and micro-topography; and further incorporate them as input parameters in the spatial-explicit hydrological model (Section 2.5). To this aim the aerial part of the vegetation patch was clipped at about 1 cm height to allow observation of overland flow advances, and water was supplied to a small area (2.5–12.2 cm^2) at the center of each plot ($n = 12$) with a single nozzle at rates (13.5–26.5 mm min^{-1}) sufficient to generate a thin laminar overland flow that would reach some border of the plot within an interval of 15–30 min. The water inflow ($W(t)$, mm^3 s^{-1}) rate was set as time-constant for each plot experiment. This parameter was determined for each field overland flow experiment by collecting the water inflow volume during one minute and estimating the corresponding inflow rate.

The runoff-plume (RP) advances beyond the application area were video-recorded with a digital camera at 1 m above the plot. All overland flow was infiltrated within the plot areas at the end of the experiments.

Antecedent soil moisture content (θ_v) (depth: 0–30 mm) was measured before application of water at an immediate neighbor location (at the border of the plot) by means of a TDR (Time-Domain Reflectometer, TRIME®-FM, Ettlingen) with an inclined pin probe (50 mm) and a gravimetric soil moisture measurement. These moisture estimates were used as input antecedent soil moisture ($\theta_{v,t=0}$) to estimate a water mass balance model of the flow experiments. The post-inflow volumetric soil moisture (θ_v) (depth: 0–30 mm) under the RP area was also measured by means of the TDR at equidistant (30–35 mm) points of a grid covering the area immediately after the water inflow ceased. The TDR estimates were calibrated with an independent set of gravimetric soil moisture measurements by extracting 3 soil cores (diameter: 4 cm, depth: 0–3, 3–9, 9–18 cm) along the RP immediately after the water inflow ceased.

A Digital Elevation Model (DEM) of each plot was built through a close-range stereo-photogrammetry and geo-statistical procedure (Rossi and Ares, 2012a). Video scenes of the RP areas were selected at specific time intervals (1–4 min, depending on the total duration of the flow experiments), exported to an image processing application (Idrisi v. 14.02, Clark Labs, Worcester), ortho-rectified, and used to estimate the increments of the RP areas:

$$\Delta A(t) = A(t_{n+1}) - A(t_n)/A_{end} \quad (3)$$

where $\Delta A(t)$ is the RP area advanced during the *n-th* interval (mm^2), $A(t_n)$ is the successive instantaneous runoff plume area (mm^2) and A_{end} is the RP area (mm^2) at the end of the flow experiment. The $A(t_n)$ and $\Delta A(t)$ overlaid to their corresponding DEM were then used to estimate the following micro-topographic flow resistance parameters and variables:

- *DS:* fraction of the RP area occupied by depression storage (*DS*, %) as calculated by Rossi and Ares (2012b). To identify the part of the RP area where depression storage occurred, the areas where the RP advanced in counter- slope direction (due to inundation of a micro-depression) were identified, measured at each time interval and further used to compute the accumulated ponded areas at the end of the experiment. (Also see Supplementary data 2.)
- σ_s*:* surface roughness of the ground calculated as the standard deviation of the terrain height change along the contour of the RP at each time interval (t_{n+1}, t_n) (mm):

$$\sigma_s = \left(\sum_{t=1}^{t=end} \left(s(t_n) - s^* \right)^2 \right) \Big/ n \quad (4)$$

where $s(t_n)$ is the terrain height change along the contour of the RP area at time t (mm), and s^* is the average terrain height change along the contour of the RP (mm) estimated at the patch and surrounding bare soil area:

$$s^* = \sum_{t=1}^{t=end} (s(t_{n+1}) - s(t_n))/n \quad (5)$$

The instantaneous overland flow at *n-th* time interval ($Q_o(t)$) was estimated as:

$$Q_o(t) = A(t) \times d(t) \quad (6)$$

where $A(t)$ is the instantaneous RP area at time t and $d(t)$ (mm) is the average depth of the RP at time t, flowing at varying velocity depending on the local altitude gradient along its border. This relation would follow Darcy's general form of the frictional law (Dingman, 2007; Mügler et al., 2011):

$$d(t) = (W(t)/C)^2/(s(t_{n+1}) - s(t_n)) \quad (7)$$

where the velocity term is replaced in this case with the (known time-constant) water inflow rate $W(t)$, and $s(t_{n+1}) - s(t_n)$ was obtained from successive video images of the RP overlaid on the plot DEMs (see Eq. (5)). The term C is a proportionality constant estimated through inverse modeling of the continuity equations shown in Fig. 3, by numerical integration with a fourth-order

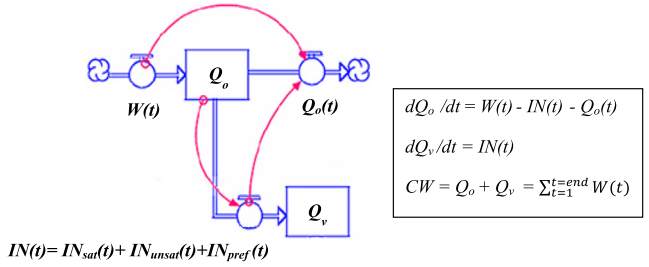

Fig. 3. Flow-stock structure and water mass balance equations of overland flow experiments. Stocks (rectangles): Q_o (water stored at the RP as overland flow); Q_v (water infiltrated at the upper vadose zone). Flows (blue circles-arrows): $IN(t)$ (instantaneous total infiltration flow); $Q_o(t)$ (instantaneous overland flow); $IN_{sat}(t)$ (instantaneous saturated infiltration flow); $IN_{unsat}(t)$ (instantaneous unsaturated infiltration flow). Red arrows represent control equations among components of the model. (For interpretation of the references to color in this figure legend, the reader is referred to the web version of this article.)

Table 1
Measured parameters and variables used to validate water mass balance equations.

	Parameters and variables	Units	Measured by
1	$A(t)$	mm^2	Areas from the video scenes of the RP
2	A_{end}	mm^2	
3	Average runoff velocity	$mm\ s^{-1}$	Areas from the video scenes and final time
4	K_{sat}	$mm\ s^{-1}$	TDI
5	s^*	mm	Plot DEM
6	*DS*	%	Plot DEM and RP advances (Rossi and Ares, 2012b)
7	θ_{end}	$mm^3\ mm^{-3}$	TDR
8	z_f	mm	Soil core samples

Runge–Kutta approximation, at solution time intervals $0.06 \leqslant \Delta t \leqslant 0.3$ s. This parameter estimation involves a bootstrap calibration by matching measured field data (field parameters–variables in Table 1) within the constraints given by the soil properties, the inflow rate and duration of the experiment. The goodness of calibration was tested through the attained water mass balance error, Nash–Sutcliffe's efficiency criteria and correlation coefficients (R^2) of observed-modeled time series of the overland flow area A and the soil moisture depth at the end of the flow experiment (θ_{end}). Once C is estimated, $d(t)$ is calculated with Eq. (7).

The average depth of the RP (d^*) was estimated at the patch and surrounding bare soil area:

$$d^* = \sum_{t=1}^{t=end} (d(t_{n+1}) - d(t_n))/n \quad (8)$$

where $d(t_n)$ is the average depth of the RP (mm) at the time t and d (t_{n+1}) is the successive average depth of the RP (mm); all calculated with Eq. (7).

The dimensionless Reynolds number (Re) of the overland flow was also estimated at the patch and surrounding bare soil area:

$$Re = 4 \cdot v^* \cdot d^*/\upsilon \quad (9)$$

where υ is the kinematic viscosity of the fluid ($0.9\ mm^2\ s^{-1}$) and v^* is the mean overland flow velocity ($mm\ s^{-1}$) calculated as:

$$v^* = (A_{end})^{0.5}/t_{end} \quad (10)$$

2.4. Dynamic water mass balances

Dynamic water mass balances at the overland flow experiments were used to calculate the masses of water involved in overland and infiltration flows, accounting for the simultaneous effects of infiltration, frictional effects and depression storages along the RP path and speed. To this aim, a set of time varying differential equations of the flow components was solved through Stella (v9.0, Isee Systems, Inc., Lebanon) application. The algorithm (Fig. 3) is based on previous work of Rossi and Ares (2012b) on a similar experimental setup at bare soil inter-patches.

The water inflow ($W(t)$, $mm^3\ s^{-1}$) rate was set as time-constant for each plot experiment. This parameter was determined for each overland flow experiment by collecting the water inflow volume during one minute and estimating the corresponding inflow rate. The instantaneous overland flow ($Q_o(t)$) changes with time as the RP plume travels on the soil surface because of variable friction generated by the surface roughness and the occurrence of depression storage (*DS*) areas where water temporarily accumulates. At some areas the RP layer is discontinuous because the water inflow is not enough to compensate infiltration. As a consequence of these, $IN(t)$ results from the composition of flows under both saturated or unsaturated conditions. Saturated conditions occur at *DS*

areas, while both saturated and/or unsaturated infiltration flows can occur at other areas depending on the presence of free water at the soil surface and/or the amount of water contained in the subsurface soil.

The saturated infiltration flow (IN_{sat}), was assumed to be restricted to ponded areas, and was estimated through the Green–Ampt's algorithm (Green and Ampt, 1911), depending on the K_{sat} estimated with the TDI (Eq. (1)) and the gradient of water head between the soil surface and a point at the infiltrating wetting front as:

$$IN_{sat} = K_{sat} \times \left[\psi_f \times \left(\frac{\theta_s - \theta(t)}{F}\right) + 1\right] \times A_{DS} \quad (11)$$

where K_{sat} is the saturated hydraulic conductivity (mm s^{-1}), $\psi_f(\theta)$ is the suction at the wetting front (mm), θ_s and $\theta(t)$ are the saturation and instantaneous volumetric water content at the wetting front respectively (mm^3 mm^{-3}), F is the accumulated infiltration (mm), $z_f(t)$ is the instantaneous water infiltration depth (mm) and A_{DS} is the DS area (mm^2).

Water infiltration was assumed to occur under unsaturated conditions in areas of the overland plume where no DS occurs.

$$IN_{unsat}(t) = K_h(\theta(t)) \times \left[\psi_f(\theta(t)) \times \left(\frac{\theta(t) - \theta_i}{F}\right) + 1\right] \times (A(t) - A_{DS}) \quad (12)$$

where $K_h(\theta(t))$ is the variable hydraulic conductivity (mm s^{-1}) and θ_i is the antecedent water content of the soil (mm^3 mm^{-3}).

$K_h(\theta(t))$ and $\psi_f(\theta(t))$ were estimated through the solution (van Genuchten, 1980) of Mualem's (Mualem, 1976) formulation to predict the relative hydraulic conductivity from knowledge of the soil–water retention curve. Parameters corresponding to residual volumetric moisture (θ_r), saturated moisture content (θ_s), tortuosity connectivity (L) and shape of the soil moisture–water head function ($\log_{10}\alpha$, $\log_{10}n$) (van Genuchten, 1980) were estimated based on the textural data of the soil cores (see Section 2.2) through pedotransfer functions (Rosetta v. 1.2, US Salinity Laboratory, Riverside) developed by Schaap and Leij (1998).

The water mass balance equations were calibrated to satisfy the (observed) time series of the overland flow areas and infiltration depths and other parameters in Table 1. The estimation of the constant C (Eq. (7)) was achieved through minimizing parameters 2–8:

$$\sum_{1}^{n}(x_{est} - x_{data})^2 = min \quad (13)$$

where x_{est} is the parameter estimate and x_{data} is the corresponding experimental-measured value.

The goodness of fit between the estimated and measured time series of the RP area (variable 1, $A(t)$) was assessed with the Nash–Sutcliffe's efficiency coefficient (EC $\geqslant$ 0.96) (Nash and Sutcliffe, 1970).

Post irrigation soil moisture TDR estimates (parameter 7, θ_{end}) were used to create upper soil moisture maps of the overland plumes of each plot experiment, based on a nearest neighbor interpolation algorithm (Richards, 1986). The water (maximum) infiltration depths (variable 8, z_f) were estimated immediately after the water inflow ceased by measuring the depth of the wetting front in the soil samples extracted along the flow trace of the RP.

2.5. Spatial-explicit simulation of overland flow within patches under natural rainfall conditions

A modified version (Rossi and Ares, 2015) of the CREST (Coupled Routing and Excess Storage) distributed hydrological model (Wang et al., 2011) was calibrated with results of four independent overland flow experiments (see Supplementary data 1) not used to compute other results here shown. The model simulates field cell-to-cell spatio-temporal variations of land surface water fluxes, infiltration and storages of water in the upper soil under various conditions of rainfall and evapotranspiration.

Stemflow and throughfall as estimated by Cecchi et al. (2006) and Martinez-Meza and Whitford (1996) corresponding to typical rain events and antecedent soil moisture conditions in the Patagonian Monte were applied to a sample plant patch area (Plot 1). The percentage of rainfall partitioned as stemflow for an individual shrub (*L. divaricata* with 0.16 m^2 canopy area) was assumed to be 7.2%, as measured by Cecchi et al. (2006) in Southern Argentina. Because there are no available throughfall measurements for this or other similar species in Southern Argentina, the percentage of rainfall partitioned as throughfall was assumed to be 55%, as measured by Martinez-Meza and Whitford (1996) in Chihuahuan desert shrubs.

The input parameters to CREST model (infiltration, soil microtopography, soil hydraulic conductivity, depression storage and overland flow metrics) were estimated through sampling soil properties at the field overland flow experiments (Sections 2.2 and 2.3) and their water mass balance modeling estimates (Section 2.4).

The CREST model outputs (overland flow paths-depths, soil moisture depths) were digitized with the Idrisi (v. 14.02, Clark Labs, Worcester) application to ease visualization.

3. Results

3.1. Soil properties

The amount of roots (SR) in the upper soil (3–9 cm) varied according to the position within the vegetation patch. SR in the soil samples extracted at the vegetation patches were in all cases higher than the SR at the immediate surrounding bare soil areas (Table 2). A significant ($P \leqslant 0.01$) positive correlation was observed between the average roughness at the soil surface (σ_s) and the amount of roots in the soil at 0–18 cm depth at the vegetation patches (Fig. 4).

The bulk density measured at the vegetation patches was lower than that at the immediate surrounding bare soil (1.2 and 1.5 g cm^3, Student t test, $P \leqslant 0.05$). Mean K_{sat} values estimated at the center of vegetation patches (0.0177 mm s^{-1} or 63.7 mm h^{-1}) were significantly higher (Student t test, $P \leqslant 0.05$) than those at the immediate surrounding bare soil (0.0063 mm s^{-1} or 22.7 mm h^{-1}).

Table 3 shows the results of a multiple regression analysis relating the amount of roots (SR) and gravel (SG) in soil and the mean K_{sat} (TDI) within the plant patches. Increasing SR (3–9 cm) values are significantly related to increasing K_{sat} (TDI) while increasing SG (0–3 cm) correspond to decreasing hydraulic conductivity.

3.2. Overland flow experiments and estimates

Fig. 5 shows examples of the spatial distribution of the soil (0–30 mm) volumetric moisture content as indicator of the extent of RP at the end of inflow periods. The RP areas occupied the top of the vegetation patch area around the inflow center, progressing into the neighbor area or immediate BS surrounding the plant patch.

Table 4 shows the quantitative agreement between the measured and estimated variables and parameters used in water mass balances. The Nash–Sutcliffe's efficiency coefficient of the modeled and estimated time series $A(t)$ was in all cases EC $\geqslant$ 0.95 (Nash and Sutcliffe, 1970). The modeled average z_f values were in all cases lower than those observed at the field. This is attributable to the fact that $z_{f\ data}$ were estimated based on the soil cores (S1, S2 and

Table 2
Amounts of roots in soil (*SR*) sampled (depth interval: 3–9 cm) at 12 vegetation patches. Samples S1 and S2 correspond to the plant patch area, S3 correspond to the bare soil area surrounding the patch.

		P01	P02	P03	P04	P05	P06	P07	P08	P09	P10	P11	P12
SR (%)	S1	0.07	0.07	0.02	0.05	0.17	0.26	0.03	0.10	0.07	0.23	0.02	0.10
	S2	0.05	0.05	0.02	0.05	0.14	0.10	0.02	0.02	0.06	0.04	0.03	0.12
	S3	0.02	0.03	0.01	0.02	0.06	0.06	0.00	0.01	0.05	0.02	0.01	0.01

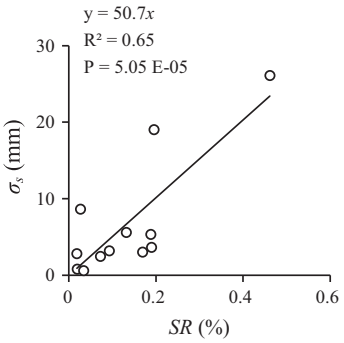

Fig. 4. Regression analysis between surface roughness (σ_s) and amount of roots in soil (*SR*, 0–18 cm depth).

Table 3
Multiple linear regression analysis between K_{sat} measured with the TDI and the sampled soil properties: Roots (*SR*) < Gravel (*SG*) (R^2 = 0.55, Df = 21, $P \leqslant 0.05$).

	β Coefficient		*t* Value	*P*
	Non standardized	Standardized		
Intercept	0.01		4.09	0.001
SR (3–9 cm)	0.068	0.67	4.36	0.000
SG (0–3 cm)	0.000	−0.30	−1.96	0.065[a]

[a] Outside the range of $P < 0.05$.

S3) located along the RP where infiltration is at a maximum, while $z_{f\ model}$ expresses the average infiltration depth corresponding to the whole RP area.

At all plots, *Re* mean values were higher at the plant patches than at the immediate surrounding bare soil areas (Fig. 6a). Except for plots 4 and 9 where no *DS* areas occurred within the vegetation patches, mean *DS* values at the plant patches were higher than those estimated at the immediate surrounding bare soil area (Fig. 6b). The volumetric soil moisture (θ_v) at the end of the flow experiments was higher at the patch areas than at the immediate surrounding bare soil (Fig. 6c). The overland flow depth (d^*) and the average terrain height change along the contour of the RP (s^*) estimates vary at the plant patches as compared with the immediate surrounding area (Fig. 6d and e).

3.3. Spatial-explicit simulation of rainfall event

Fig. 7 shows an example of computer simulations with CREST solved at a high spatial resolution (*x*–*y*: 50 mm: *z*: 1 mm) with model parameters corresponding to the field overland flow and infiltration estimates at Plot #1 (W: −64.98465; S: −42.2064333) in this study. This is a plot with a spotted vegetation-related mound dominated by *L. divaricata Cav.* and *P. speciosae* on a nearly flat general slope. CREST results of overland flows are depicted overlaid on a rectified image of the plot and a map of the contour lines of topographic elevation. Throughfall has been simulated to

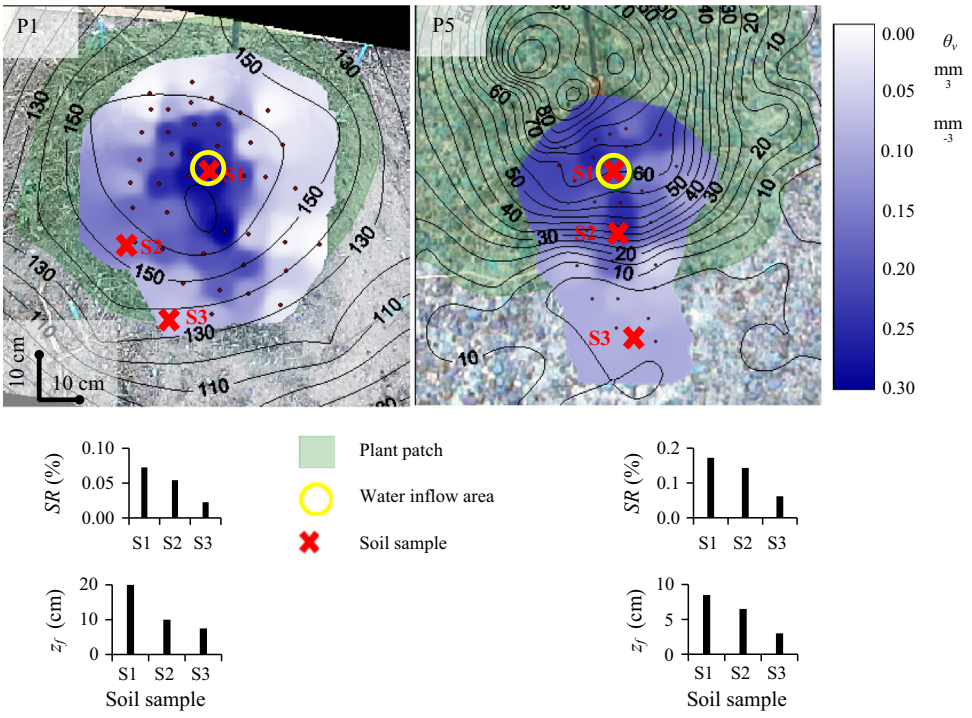

Fig. 5. Map of soil (0–30 mm) volumetric moisture content (θ_v) as indicator of the extent of the runoff plume at plots 1 and 5 at the end of the water inflow period. Black dots indicate the TDR probing points. The maps are overlaid on a rectified cenital photo of the plot and corresponding digital elevation map with contour lines of topographic elevation (mm). Lower insets: Amount of roots in soil (*SR*) and water infiltration depth (z_f) sampled along the trace of the RP. Samples S1 and S2 correspond to the plant patch area, S3 correspond to immediate surrounding bare soil.

Table 4
Measured and calibrated parameters–variables in water mass balance estimates of overland flow experiments.

	P1	P2	P3	P4	P5	P6	P7	P8	P9	P10	P11	P12	R^2
$A(t)$ (mm^2)[a]	0.993	0.997	0.965	0.990	0.994	0.996	0.997	0.961	0.972	0.982	0.986	0.991	
A_{end} (mm^2)	1.8E+05	7.0E+04	7.3E+04	1.6E+05	1.4E+05	2.0E+05	1.1E+05	1.7E+05	8.7E+04	1.9E+05	1.3E+05	1.7E+05	0.998
	1.8E+05	**7.0E+04**	**7.4E+04**	**1.6E+05**	**1.4E+05**	**2.0E+05**	**1.1E+05**	**1.7E+05**	**8.8E+04**	**1.9E+05**	**1.3E+05**	**1.7E+05**	
Average runoff velocity (mm s^{-1})	0.27	0.85	0.59	0.68	0.86	1.56	1.89	0.55	0.48	0.97	0.45	1.30	0.999
	0.27	**0.85**	**0.60**	**0.67**	**0.86**	**1.56**	**1.89**	**0.55**	**0.49**	**0.97**	**0.45**	**1.28**	
K_{sat} (mm s^{-1})	1.21E−02	8.35E−03	7.10E−03	5.70E−03	1.48E−02	1.10E−02	7.20E−03	1.47E−02	3.05E−02	1.25E−02	6.60E−03	1.14E−02	0.999
	1.21E−02	**8.35E−03**	**7.10E−03**	**5.70E−03**	**1.48E−02**	**1.10E−02**	**7.20E−03**	**1.57E−02**	**3.05E−02**	**1.25E−02**	**8.55E−03**	**1.31E−02**	
s^* (mm)	1.93	2.86	2.31	2.13	4.01	4.06	8.18	3.86	2.83	4.42	3.54	7.74	0.999
	1.92	**2.86**	**2.28**	**2.10**	**4.01**	**4.04**	**8.25**	**3.92**	**2.83**	**4.44**	**3.35**	**7.75**	
DS (%)	16.62	10.99	12.40	0.13	7.55	10.15	7.59	10.24	0.77	10.18	14.32	14.25	0.925
	16.30	**10.89**	**16.72**	**0.12**	**9.91**	**12.44**	**8.57**	**12.18**	**0.00**	**10.88**	**16.60**	**19.73**	
σ_s (mm)	2.33	5.86	1.13	0.66	15.47	2.87	27.99	4.09	2.89	8.58	1.64	12.56	0.999
	2.46	**6.18**	**1.22**	**0.67**	**15.45**	**3.16**	**28.42**	**4.01**	**2.88**	**8.70**	**1.73**	**12.74**	
θ_{end} (mm^3 mm^{-3})	0.20	0.21	0.15	0.15	0.20	0.15	0.17	0.18	0.15	0.17	0.18	0.13	0.922
	0.19	**0.21**	**0.15**	**0.16**	**0.21**	**0.15**	**0.16**	**0.18**	**0.15**	**0.16**	**0.20**	**0.12**	
z_f (mm)	87.0	42.0	70.0	30.0	43.0	34.0	20.0	58.0	68.0	65.0	67.0	53.0	0.972
	125.0	**64.3**	**99.0**	**40.0**	**60.0**	**43.3**	**28.3**	**69.7**	**96.7**	**90.0**	**90.8**	**66.0**	
Water mass balance error (mm^3)	5E−10	2E−10	3E−10	1E−10	5E−10	1E−10	−1E−10	5E−10	3E−10	2E−10	3E−10	−3E−10	

Data in bold correspond to field measurements.
[a] Goodness of fit assessed in terms of the Nash–Sutcliffe's efficiency coefficient.

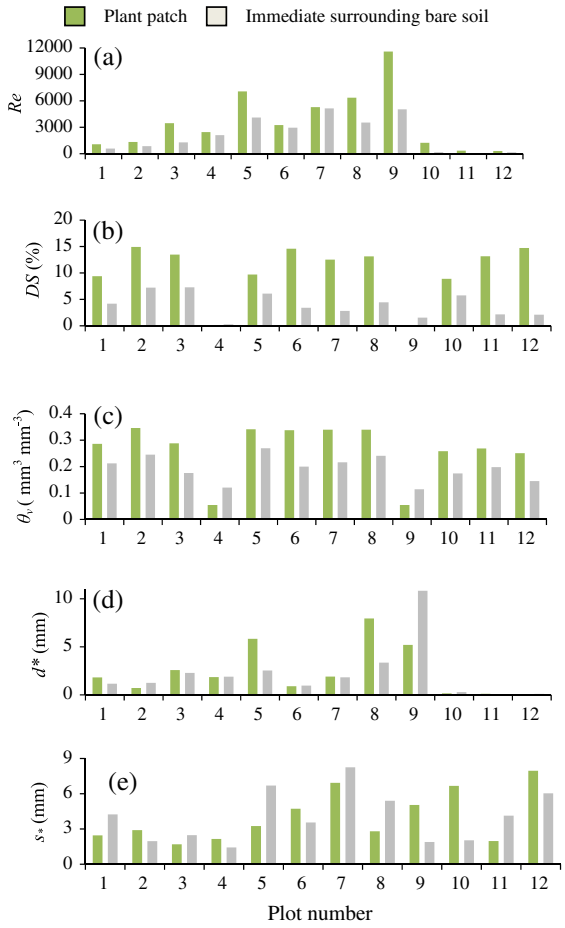

Fig. 6. (a) Reynolds number (Re), (b) depression storage (DS), (c) volumetric moisture content (θ_v), (d) average depth of the runoff plume (d^*) and (e) average terrain height change along the contour of the runoff plume (s^*) estimated at plant patch areas and immediate surrounding bare soil.

occur at the entire patch area while stemflow has been assumed to occur at a small central area of the vegetation patch. The results correspond to overland flow depth and infiltrated soil moisture at times during a rainfall event on nearly dry soil as feasible during Summer at the Patagonian Monte area. The flow generated by stemflow and throughfall at the plant patch reached the immediate surrounding bare soil area after 30 min of rain start. Unusually heavy Summer rains as recorded at local gauges may last up to 1 h.

4. Discussion

4.1. Overland flow experiments and soil properties

In previous flow experiments, the main purpose is to observe and characterize the behavior of laminar flows on vegetated or bare soil areas. As different from rainfall simulation experiments where nominal rainfall rates are mimicked, flow studies utilize high water inputs relatively un-related to the naturally occurring instantaneous rainfall input (Wang et al., 2011). For instance, Abrahams et al. (1990) used trickles to supply 572 cm^3 s^{-1} to the top of 10 m^2 plots in studies of flow resistance in semi-arid environments, while Dunkerley (2003) choose perforated pipes to deliver 10–90 cm^3 s^{-1} to laboratory plots of 1.4 m^2. Similarly, the use of controlled water inflow through drippers, perforated pipes, etc. at the top of the plots (Dunkerley, 2001, 2003; Hessel et al., 2003) has also been found suitable to simulate stem flow at

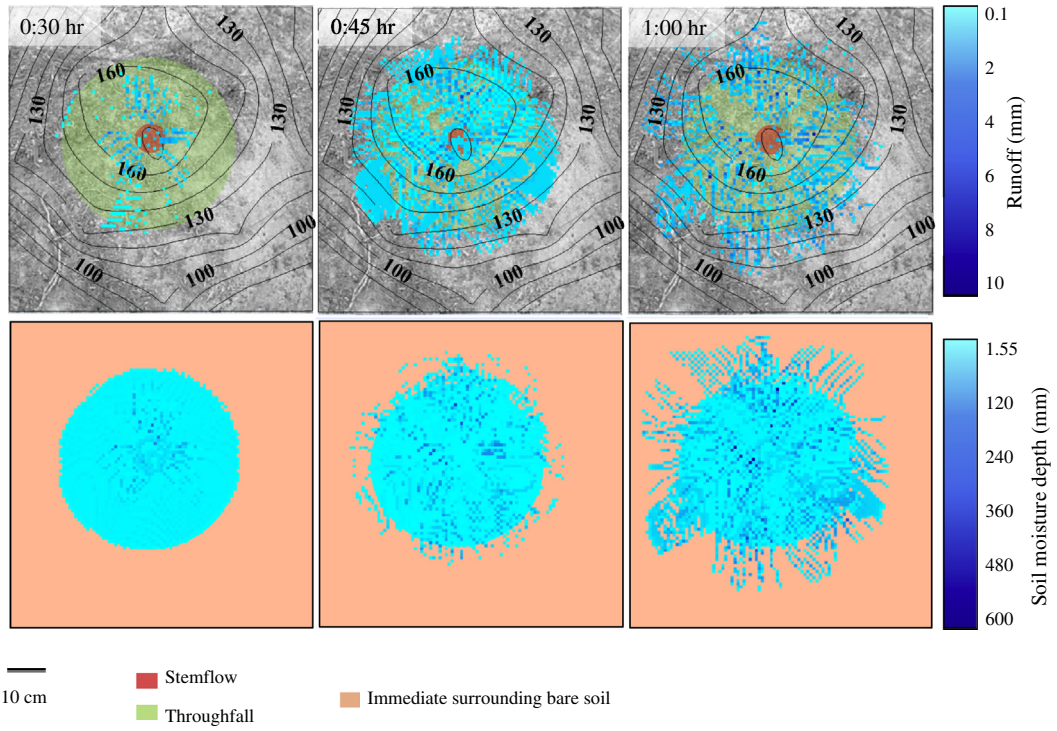

Fig. 7. Simulation results (CREST model) of overland flows (direction, flow depth) and soil moisture depth (low insets) at a plant patch area (Plot 1) resulting from stemflow and throughfall during a Summer-rain event at the Patagonian Monte (44 mm h^{-1}, θ_i: 1.5 mm). Results are overlaid on a photograph of the plot and a map of contour lines of topographic elevation (mm).

vegetated plots. Flow friction factors measured at flow plots have been used as input parameters at coarser distributed parameter runoff models (Howes and Abrahams, 2003).

Infiltration experiments and models aimed to simulate non-uniform overland flows across dryland soil surfaces used technical surfaces to mimic overland flows (Dunkerley, 2003), flume experiments at laboratory conditions with no infiltration (Chu et al., 2013) or uniform infiltration conditions (Strohmeier et al., 2014) and field experiments over plots including various forms of plant patches interspersed with bare soil (Chen et al., 2013; Li et al., 2008; Michaelides et al., 2009; Reid et al., 1999). The results here presented were obtained on vegetated plant patches, under simultaneous and dynamically varying preferential infiltration. The estimation of the frictional (flow speed, laminar depth, depression storage) characteristics of the overland flow were consistent with the water mass-balance at the experimental flow.

The higher bulk density in the soil surrounding plant patches as compared to the same inside the patches has been attributed to soil compaction resulting from the erosive force of rainfall drops affecting soil detachment (Ekwue and Harrilal, 2010; Römkens et al., 2002). Lower bulk density in the plant patch area is attributed to the positive influence of vegetation on their microenvironment, through the improvement of soil properties under their canopy (Bedford and Small, 2008; Bochet et al., 1998; Michalet et al., 2015).

Reynolds numbers (*Re*) and depression storages (*DS*) are in most cases higher at the plant patch area than in near surrounding soil (Fig. 6a and b). This is consistent with the positive correlation observed between the soil root content (as indicator of the density of the plant patch) and the heterogeneity of the micro-relief as indicated by the variance of terrain height within the plant patch (Martin et al., 2008). Higher *Re* mean values at the plant patch areas were also attributed to the flow turbulence caused by plant stems (Rogers and Schumm, 1991).

Few measurements of depression storage under natural conditions actually exist, and it is typically dealt with as a fitting parameter to calibrate hydrological models to reproduce observed runoff flows (Richards et al., 2013). Most work on depression storage has focused strictly on bare soil in flume and plot studies (Darboux and Huang, 2005; Onstad, 1984; Rossi and Ares, 2012b). Studies that have explicitly examined depression storage in connection with vegetation were conducted in coffee fields (Lin and Richards, 2007), wetlands (Frei and Fleckenstein, 2014) and ex-urbanizing landscapes (Richards et al., 2013). It has been assumed that water infiltration occurs under saturated conditions at areas of depression storage (Rossi and Ares, 2012b).

The presence of vegetation or litter increases the friction encountered by water flowing under the shrubs (Howes and Abrahams, 2003). The heterogeneity of micro-relief increases the sinuosity-turbulence of the overland flow and creates suitable places for water storage. This enhances infiltration at the patch area, which in turn results in higher volumetric moisture content as compared with the immediate surrounding area (Figs. 5 and 6a–c). Considering a capillary velocity of 0.029 mm s^{-1} (Lu and Likos, 2004), and that the volumetric soil moisture was measured 2–3 min after the water inflow ceased, the increased soil moisture would have extended laterally 3.48–5.22 mm from the border of the RP. Therefore there was no sufficient time for considerable dispersion in the subsurface, and the extent of the volumetric moisture content would match well with the extent of the RP at the surface at the end of the inflow period.

The pattern of overland flow depth (d^*) and the average terrain height change along the contour of the RP (s^*) variation from the patch area to the immediate surrounding soil area (Fig. 6d and e) depends on the shape (curvature) of the plant patch slope as characterized through the ratios $d^*_p/d^*_b - s^*_p/s^*_b$ where the suffixes p, b refer to patchand bare soil area respectively (Fig. 8). According to the d^* ratio with respect to the s^* ratio, plant patches can be

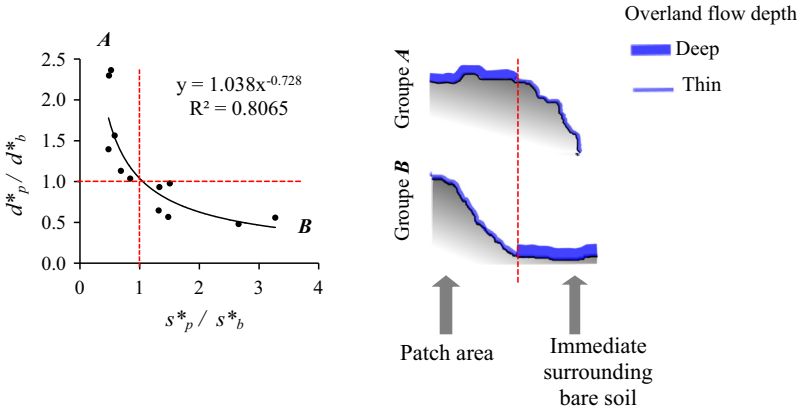

Fig. 8. Left inset: Classification of plant patches according to their convexity with respect to the terrain height change between the central area of the patch and its surroundings. $s^*_p/s^*_b = d^*_p/d^*_b = 1$ corresponds to flat patch areas. Right inset: Schematic representation of shape of the plant patch slope and its effect on overland flow depth.

classified in: *A* (convex) and *B* (concave) types. The d^* estimates of group *A* (plots 1, 3, 5, 7, 8 and 11) are higher at the plant patches than those estimated at the immediate surrounding area. The opposite is observed at plots of group *B* (2, 4, 6, 9, 10 and 12).

The results of the regression analysis (Table 3) are compatible with the hypothesis that the amount of roots (*SR*) and gravel (*SG*) are the most important soil properties affecting K_{sat} (TDI) within the plant patches. As in other studies (Li et al., 2008; Novák et al., 2011; Poesen and Ingelmo-Sanchez, 1992; Poesen and Lavee, 1994) it is probable that rock fragments embedded in the soil surface participate in establishing a continuous crust inhibiting infiltration. A negative effect of soil rock fractions on infiltration has been assumed in modeling soil conductivity (Novák et al., 2011).

4.2. Use of flow plot parameters in distributed hydrological modeling

The results of surface water flows and storage of water in the upper soil produced by the CREST model confirms that overland flow can occur originated by stemflow and throughfall at the plant patch areas during usual storms at the Patagonian Monte. The intensity of surface flows, the time at which the flows reach the surrounding bare soil and the relative importance of stemflow–throughfall partition may depend on the regime of the storm and the soil antecedent moisture (Ferrante et al., 2014).

Typical Summer storms seldom last more than 0:30 h, although longer and deeper storms have been occasionally recorded (Puerto Madryn Port Administration, http://www.appm.com.ar). In the case of these unusual heavy rainfall events, overland flow (both throughfall and stemflow-fed) is expected to diverge from mound-related spotted plant patches and extend over the immediate surrounding BS areas.

These results indicate that under circumstances, eventual but intense overland flows can occur from the plant patches to surrounding soil areas. During these events, litter and sediments can be transported from the relatively nutrient rich patch areas to the nearby soil, as also confirmed by the occurrence of rills and dikes around the periphery of plant patches in patterns independent of the main slope (Fig. 1).

5. Conclusions

The results here shown highlight the complexity of the interactions of soil micro-relief, the action of vegetation in the development of mounds at plant patches, and their effects on water infiltration under shallow or relatively deeper overland flow. Overland flow metrics vary within different areas of the plant patches depending on the shape of their peripheral slopes. It is shown that these variations are relevant in considering the infiltration capacity of patches and their role in surface water redistribution.

Empirical evidence shows that water transport from plant patch areas toward the immediate surrounding bare soil occurs in semi-arid areas of the Patagonian Monte. The results of spatial-explicit hydrological simulation show that water transport can result from stemflow and throughfall at the patch areas during typical rainfall events. Implications of this phenomenon in the surface distribution of water, nutrients and seeds may feasibly follow. These are the subject of continuing research at our laboratory.

Acknowledgements

This study was supported by grants of Agencia Nacional de Investigaciones Científicas y Técnicas (ANPCyT) PICT13-1368. M.J. Rossi is a postdoctoral fellow on leave from National Patagonic Center.

Appendix A. Supplementary material

Supplementary data associated with this article can be found, in the online version, at http://dx.doi.org/10.1016/j.jhydrol.2015.12.028.

References

Abraham, E., del Valle, H., Roig, F., Torres, L., Ares, J., Coronato, F., Godagnone, R., 2009. Overview of the geography of the Monte desert of Argentina. J. Arid Environ. 73, 144–153.

Abrahams, A.D., Parsons, A.J., Luk, S., 1990. Field experiments on the resistance to overland flow on desert hillslopes, Erosion, Transport and Deposition Processes. In: Proceedings of the Jerusalem Workshop, March–April. IAHS Publ. No. 189, Jerusalem, 1990.

Abrahams, A.D., Parsons, A.J., Wainwright, J., 2003. Disposition of rainfall under creosotebush. Hydrol. Process. 17, 2555–2566.

Archer, N., Quinton, J., Hess, T., 2012. Patch vegetation and water redistribution above and below ground in south east Spain. Ecohydrology 120, 108–120.

Ares, J.O., Beeskow, A.M., Bertiller, M.B., Rostagno, M., Irisarri, M., Anchorena, J., Defossé, G.E., Merino, C.A., 1990. Structural and dynamic characteristics of overgrazed lands of northern Patagonia, Argentina. In: Breymeyer, A. (Ed.), Managed Grasslands: Regional Studies, pp. 149–175.

Bautista, S., Mayor, A.G., Bourakhouadar, J., Bellot, J., 2007. Plant spatial pattern predicts hillslope runoff and erosion in a semiarid Mediterranean landscape. Ecosystems 10, 987–998.

Bedford, D.R., Small, E.E., 2008. Spatial patterns of ecohydrologic properties on a hillslope–alluvial fan transect, central New Mexico. Catena 73, 34–48.

Bertiller, M.B., Beeskow, A.M., Coronato, F., 1991. Seasonal environmental variation and plant phenology in arid Patagonia (Argentina). J. Arid Environ. 21, 1–11.

Bisigato, A.J., Villagra, P.E., Ares, J.O., Rossi, B.E., 2009. Vegetation heterogeneity in Monte Desert ecosystems: a multi-scale approach linking patterns and processes. J. Arid Environ. 73, 182–191.
Bochet, E., 2015. The fate of seeds in the soil: a review of the influence of overland flow on seed removal and its consequences for the vegetation of arid and semiarid patchy ecosystems. Soil 1 (1), 131–146.
Bochet, E., Rubio, J.L., Poesen, J., 1998. Relative efficiency of three representative matorral species in reducing water erosion at the microscale in a semi-arid climate (Valencia, Spain). Geomorphology 23, 139–150.
Böhm, W., 1979. Methods of Studying Root Systems. Springer-Verlag, Berlin.
Bromley, J., Brouwer, J., Barker, A.P., Gaze, S.R., Valentin, C., 1997. The role of surface water redistribution in an area of patterned vegetation in a semi-arid environment, south-west Niger. J. Hydrol. 198, 1–29.
Casermeiro, M.A., Molina, J.A., de la Cruz Caravaca, M.T., Hernando Costa, J., Hernando Massanet, M.I., Moreno, P.S., 2004. Influence of scrubs on runoff and sediment loss in soils of Mediterranean climate. Catena 57, 91–107.
Cecchi, G., Kröpfl, A.I., Villasuso, N.M., Distel, R., 2006. Stemflow and soil water redistribution in intact and disturbed plants of *Larrea divaricata* in Southern Argentina. Arid Land Res. Manage. 20 (3), 209–217.
Chartier, M., Rostagno, C., 2006. Soil erosion thresholds and alternative states in northeastern Patagonian rangelands. Rangeland Ecol. Manage. 59, 616–624.
Chen, L., Sela, S., Svoray, T., Assouline, S., 2013. The role of soil-surface sealing, microtopography, and vegetation patches in rainfall–runoff processes in semiarid areas. Water Resour. Res. 49 (9), 5585–5599.
Chu, X., Yang, J., Chi, Y., Zhang, J., 2013. Dynamic puddle delineation and modeling of puddle to-puddle filling–spilling–merging–splitting overland flow processes. Water Resour. Res. http://dx.doi.org/10.1002/wrcr.20286.
Cornet, A.F., Montaña, C., Delhoume, J.P., Lopez-Portillo, J., 1992. Water flows and dynamics of desert vegetation stripes. In: Hansen, A.J., di Castri, F. (Eds.), Landscape Boundaries—Consequences for Biotic Diversity and Ecological Flows. Springer-Verlag, New York, pp. 327–345.
Couteron, P., Lejeune, O., 2001. Periodic spotted patterns in semi-arid vegetation explained by a propagation-inhibition model. J. Ecol. 89, 616–628.
Darboux, F., Huang, C., 2005. Does soil surface roughness increase or decrease particle transfers? Soil Sci. Soc. Am. J. 69, 748–756.
del Valle, H.F., Elissalde, N.O., Gagliardini, D.A., Milovich, J., 1998. Status of desertification in the Patagonian region: assessment and mapping from satellite imagery. Arid Soil Res. Rehabil. 12, 95–122.
Dingman, S.L., 2007. Analytical derivation of at-a-station hydraulic–geometry relations. J. Hydrol. 334, 17–27.
Dunkerley, D., 2013. Stemflow on the woody parts of plants: dependence on rainfall intensity and event profile from laboratory simulations. Hydrol. Process. 28 (22), 5469–5482.
Dunkerley, D.L., 2001. Estimating the mean speed of laminar overland flow using dye-injection. Uncertainty on rough surfaces. Earth Surf. Process. Landf. 26, 363–374.
Dunkerley, D.L., 2002. Infiltration rates and soil moisture in a groved mulga community near Alice Springs, arid central Australia: evidence for complex internal rainwater redistribution in a runoff–runon landscape. J. Arid Environ. 51 (2), 199–219.
Dunkerley, D.L., 2003. Determining friction coefficients for interrill flows: the significance of flow filaments and backwater effects. Earth Surf. Process. Landf. 28 (5), 475–491.
Dunkerley, D.L., Brown, K.J., 1995. Runoff and runon areas in a patterned chenopod shrubland, arid western New SouthWales, Australia: characteristics and origin. J. Arid Environ. 30, 41–55.
Ekwue, E.I., Harrilal, A., 2010. Effect of soil type, peat, slope, compaction effort and their interactions on infiltration, runoff and raindrop erosion of some Trinidadian soils. Biosyst. Eng. 105 (1), 112–118.
Ferrante, D., Oliva, G.E., Fernández, R.J., 2014. Soil water dynamics, root systems, and plant responses in a semiarid grassland of Southern Patagonia. J. Arid Environ. 104, 52–58.
Frei, S., Fleckenstein, J.H., 2014. Representing effects of micro-topography on runoff generation and sub-surface flow patterns by using superficial rill/depression storage height variations. Environ. Modell. Softw. 52, 5–18.
Gee, G.W., Bauder, J.W., 1986. Particle-size analysis. In: Klute, A. (Ed.), Methods of Soil Analysis, Part 1, Physical and Mineralogical Methods, second ed. Agronomy Monograph No. 9, ASA-SSSA.
Gill, R., Burke, I.C., Milchunas, D.G., Lauenroth, W.K., 1999. Relationship between root biomass and soil organic matter pools in the shortgrass steppe of eastern Colorado. Ecosystems 2, 226–236.
Green, W.H., Ampt, G.A., 1911. Studies on soil physics: 1. The flow of air and water through the soils. J. Agric. Sci. 4, 1–24.
Harman, C., Lohse, K., Troch, P.A., Sivapalan, M., 2014. Spatial patterns of vegetation, soils, and microtopography from terrestrial laser scanning on two semiarid hillslopes of contrasting lithology. J. Geophys. Res. http://dx.doi.org/10.1002/2013JG002507.
Hessel, R., Jetten, V., Guanghui, Z., 2003. Estimating Manning's *n* for steep slopes. Catena 54, 77–91.
Howes, D., Abrahams, A.D., 2003. Modeling runoff and runon in a desert shrubland ecosystem, Jornada Basin, New Mexico. Geomorphology 53, 45–73.
ISO 11272, 1998. Deutsches Institut für Normung – Soil Quality – Determination of Dry Bulk Density. Beuth Verlag, Berlin.
Klausmeier, C.A., 1999. Regular and irregular patterns in semiarid vegetation. Science 284, 1826–1828.
Li, X.J., Li, X.R., Song, W.M., Gao, Y.P., Zheng, J.G., Jia, R.L., 2008. Effects of crust and shrub patches on runoff, sedimentation, and related nutrient (C, N) redistribution in the desertified steppe zone of the Tengger Desert, Northern China. Geomorphology 96 (1), 221–232.
Lin, B.B., Richards, P.L., 2007. Soil random roughness and depression storage on coffee farms of varying shade levels. Agric. Water Manage. 92, 194–204.
Llorens, P., Domingo, F., 2007. Rainfall partitioning by vegetation under Mediterranean conditions. A review of studies in Europe. J. Hydrol. 335, 37–54.
Lu, N., Likos, W.J., 2004. Rate of capillary rise in soil. J. Geotech. Geoenviron. Eng., ASCE 130 (6), 646–655.
Ludwig, J., Tongway, D.J., Marsden, S.G., 1999. Stripes, strands or stipples: modelling the influence of three landscape banding patterns on resource capture and productivity in semi-arid woodlands, Australia. Catena 37, 257–273.
Malam Issa, O., Valentin, C., Rajot, J.L., Cerdan, O., Desprats, J.F., Bouchet, T., 2011. Runoff generation fostered by physical and biological crusts in semi-arid sandy soils. Geoderma 167–168, 22–29.
Mao, L.L., Lei, T.W., Li, X., Liu, H., Huang, X.F., Zhang, Y.N., 2008. A linear source method for soil infiltrability measurement and model representations. J. Hydrol. 353, 49–58.
Martin, Y., Valeo, C., Tait, M., 2008. Centimetre-scale digital representations of terrain and impacts on depression storage and runoff. Catena 75 (2), 223–233.
Martinez-Meza, E., Whitford, W.G., 1996. Stemflow, throughfall and channelization of stemflow by roots in three Chihuahuan desert shrubs. J. Arid Environ. 32 (3), 271–287.
Merino-Martín, L., Moreno-de las Heras, M., Espigares, T., Nicolau, J.M., 2015. Overland flow directs soil moisture and ecosystem processes at patch scale in Mediterranean restored hillslopes. Catena 133, 71–84.
Michaelides, K., Lister, D., Wainwright, J., Parsons, A.J., 2009. Vegetation controls on small-scale runoff and erosion dynamics in a degrading dryland environment. Hydrol. Process. 23, 1617–1630.
Michalet, R., Brooker, R.W., Lortie, C.J., Maalouf, J.P., Pugnaire, F.I., 2015. Disentangling direct and indirect effects of a legume shrub on its understorey community. Oikos. http://dx.doi.org/10.1111/oik.01819.
Moreno-de las Heras, M., Saco, P.M., Willgoose, G.R., Tongway, D.J., 2012. Variations in hydrological connectivity of Australian semiarid landscapes indicate abrupt changes in rainfall-use efficiency of vegetation. J. Geophys. Res. http://dx.doi.org/10.1029/2011JG001839.
Mualem, Y., 1976. A new model for predicting the hydraulic conductivity of porous media. Water Resour. Res. 13 (3), 513–522.
Mügler, C., Planchon, O., Patin, J., Weill, S., Silvera, N., Richard, P., Mouche, E., 2011. Comparison of roughness models to simulate overland flow and tracer transport experiments under simulated rainfall at plot scale. J. Hydrol. 402 (1), 25–40.
Nash, J.E., Sutcliffe, J.V., 1970. River flow forecasting through conceptual models; Part I. A discussion of principles. J. Hydrol. 10 (3), 282–290.
Novák, V., Kňava, K., Šimůnek, J., 2011. Determining the influence of stones on hydraulic conductivity of saturated soils using numerical method. Geoderma 161 (3–4), 177–181.
Onstad, C.A., 1984. Depressional storage on tilled storage surfaces. Trans. ASAE 27, 729–732.
Poesen, J., Ingelmo-Sanchez, F., 1992. Runoff and sediment yield from top soils with different porosity as affected by rock fragment cover and position. Catena 19, 451–474.
Poesen, J., Lavee, H., 1994. Rock fragments in top soils: significance and processes. Catena 23, 1–28.
Pueyo, Y., Moret-Fernández, D., Saiz, H., Bueno, C.G., Alados, C.L., 2013. Relationships between plant spatial patterns, water infiltration capacity, and plant community composition in semi-arid Mediterranean ecosystems along stress gradients. Ecosystems 16 (3), 452–466.
Rango, A., Tartowski, S.L., Laliberte, A., Wainwright, J., Parsons, A., 2006. Islands of hydrologically enhanced biotic productivity in natural and managed arid ecosystems. J. Arid Environ. 65 (2), 235–252.
Reid, K.D., Wilcox, B.P., Breshears, D.D., MacDonald, L., 1999. Runoff and erosion in a Pinon-Juniper woodland: influence of vegetation patches. Soil Sci. Soc. Am. J. 63, 1869–1879.
Richards, J.A., 1986. Remote Sensing Digital Image Analysis: An Introduction. Springer, Berlin.
Richards, P.L., Norris, M.D., Lin, B.B., 2013. The hydrologic implications of old field succession: depression storage and leaf litter. Ecohydrology 6 (5), 863–877.
Rogers, R.D., Schumm, S.A., 1991. The effect of sparse vegetation cover on erosion and sediment yield. J. Hydrol. 123, 19–24.
Römkens, M.J.M., Helming, K., Prasad, S.N., 2002. Soil erosion under different rainfall intensities, surface roughness, and soil water regimes. Catena 46 (2–3), 103–123.
Rossi, M.J., Ares, J.O., 2012a. Close range stereophotogrammetry and video imagery analyses in soil ecohydrology modelling. Photogramm. Rec. 27, 111–126.
Rossi, M.J., Ares, J.O., 2012b. Depression storage and infiltration effects on overland flow depth–velocity–friction at desert conditions: field plot results and model. Hydrol. Earth Syst. Sci. 16 (9), 3293–3307.
Rossi, M.J., Ares, J.O., 2015. Efficiency improvement in linear-move sprinkler systems through moderate runoff–runon control. Irrig. Sci. 33 (3), 205–219.
Schaap, M.G., Leij, F.J., 1998. Database related accuracy and uncertainty of pedotransfer functions. Soil Sci. 163, 765–779.
Silva, J.S., Rego, F.C., 2003. Root distribution of a Mediterranean shrubland in Portugal. Plant Soil 255, 529–540.

Soil Survey Staff, 1999. Soil taxonomy: a basic system of soil classification for making and interpreting soil surveys. Agricultural Handbook 436, USDA Soil Conservation Service. US Government Printing Office, Washington, DC.
Soriano, A., 1950. La vegetación del Chubut. Rev. Argent. Agron. 17, 30–66.
Strohmeier, S.M., Nouwakpo, S.K., Huang, C.H., Klik, A., 2014. Flume experimental evaluation of the effect of rill flow path tortuosity on rill roughness based on the Manning–Strickler equation. Catena 118, 226–233.
Thompson, S., Katul, G., Konings, A., Ridolfi, L., 2011. Unsteady overland flow on flat surfaces induced by spatial permeability contrasts. Adv. Water Resour. 34 (8), 1049–1058.
Thompson, S.E., Assouline, S., Chen, L., Trahktenbrot, A., Svoray, T., Katul, G.G., 2014. Secondary dispersal driven by overland flow in drylands: review and mechanistic model development. Movement Ecol. 2 (7), 1–13.
van Genuchten, M.T., 1980. A closed-form equation for predicting the hydraulic conductivity of unsaturated soils. Soil Sci. Soc. Am. J. 47 (44), 892–898.
Van Schaik, N.L.M.B., 2009. Spatial variability of infiltration patterns related to site characteristics in a semi-arid watershed. Catena 78, 36–47.
Vásquez-Méndez, R., Ventura-Ramos, E., Oleschko, K., Hernández-Sandoval, L., Parrot, J.-F., Nearing, M., 2010. Soil erosion and runoff in different vegetation patches from semiarid Central Mexico. Catena 80 (3), 162–169.
von Hardenberg, J., Meron, E., Shachak, M., Zarmi, Y., 2001. Diversity of vegetation patterns and desertification. Phys. Rev. Lett. 87 (19), 198101–198104.
Wainwright, J., Parsons, A.J., Schlesinger, W.H., Abrahams, A.D., 2002. Hydrology–vegetation interactions in areas of discontinuous flow on a semi-arid bajada, Southern New Mexico. J. Arid Environ. 51, 319–338.
Wang, X.P., Wang, Z.N., Berndtsson, R., Zhang, Y.F., Pan, Y.X., 2011. Desert shrub stemflow and its significance in soil moisture replenishment. Hydrol. Earth Syst. Sci. 15 (2), 561–567.
Wooding, R.A., 1968. Steady infiltration from a shallow circular pond. Water Resour. Res. 4, 1259–1273.